Flight phases with tests of a projectile-drone hybrid system

Patrick Gnemmi, Sébastien Changey, Pierre Wey, Emmanuel Roussel, Christian Rey, Mohamed Boutayeb, Rogelio Lozano

▶ **To cite this version:**

Patrick Gnemmi, Sébastien Changey, Pierre Wey, Emmanuel Roussel, Christian Rey, et al.. Flight phases with tests of a projectile-drone hybrid system. IEEE Transactions on Control Systems Technology, 2018, 26 (6), pp.2091-2105. 10.1109/TCST.2017.2749559 . hal-01928198

HAL Id: hal-01928198
https://hal.science/hal-01928198

Submitted on 23 Nov 2023

HAL is a multi-disciplinary open access archive for the deposit and dissemination of scientific research documents, whether they are published or not. The documents may come from teaching and research institutions in France or abroad, or from public or private research centers.

L'archive ouverte pluridisciplinaire **HAL**, est destinée au dépôt et à la diffusion de documents scientifiques de niveau recherche, publiés ou non, émanant des établissements d'enseignement et de recherche français ou étrangers, des laboratoires publics ou privés.

Flight Phases With Tests of a Projectile-Drone Hybrid System

P. Gnemmi, S. Changey, P. Wey, E. Roussel, C. Rey, M. Boutayeb, and R. Lozano

***Abstract*— A fully functional prototype of a gun-launched micro air vehicle system (GLMAV) is developed for long-distance observation capabilities. A subsonic projectile is launched from an ad hoc tube and transforms into a micro air vehicle (MAV) once arrived over the site to be observed. The ballistic, transient, and operational flight phases of the GLMAV are studied theoret-ically and experimentally in this paper. Ballistic flight tests prove the stability of the platform in projectile mode and the availability of the inertial measurement unit and GPS measurements for the autopilot. Based on wind-tunnel measurements, a model of the transient phase is built, allowing the design and simulation of control laws for this phase. Indoor and outdoor tests of the system are successfully achieved highlighting the hovering and maneuvering flight capabilities of the GLMAV.**

***Index Terms*— Counter-rotating rotors, hovering flight autopi-lot, launched micro air vehicle (MAV), miniature drone, subsonic projectile.**

I. Introduction

A ROTARY-WING micro air vehicle (MAV) has the ability to perform hover flights, contrary to a fixed-wing MAV. This hovering flight capacity is a real advantage for close and detailed observation over a site or through a window of a building. However, the long flight duration to bring a rotary-wing MAV over a site to be observed is a drawback, compared to a fixed-wing MAV. The concept of a hybrid system such as the gun-launched MAV (GLMAV) is proposed to overcome this drawback. The GLMAV concept consists of a projectile launched by an *ad hoc* small-sized cannon which is transformed into a miniature drone with automatic deployment of coaxial counter-rotating rotors after the ballistic flight. The vehicle in drone configuration is slowed down until it is able to execute hovering and/or maneuvering flights for observation purposes. A literature review published in 2008 already showed numerous smart systems involving projectiles, unmanned air vehicles (UAVs), and MAVs [1], [2].

Most studies dealing with smart hybrid projectiles or UAVs/MAVs belong to an extended range of ammunition, such as in [3]–[10]. These are high-velocity vehicles; therefore, they have no hovering capability, as they are not dedicated to this type of mission, unlike the proposed solution.

A more recent survey on hybrid systems involving a launch-ing phase and a classical flight phase is reported in [11]. A rotochute is designed as an aerodynamic decelerator [12]. The proposed prototype is a gun-launched projectile equipped with folded blades connected to the fuselage. The blades are deployed near the apogee to reduce the falling velocity. The rotochute is not controlled and operates on the autorotation principle of a helicopter. From 2012 onward, several other concepts of gun-launched hybrid MAVs have been success-fully developed, mainly for observation purposes [13]–[16]. However, all these prototypes are based on a fixed-wing architecture. A more comprehensive review given in [2] shows that no vehicle with a similar working principle to the GLMAV exists on the market. The launching phase only serves for the initialization of the MAV flight at the appropriate velocity ensuring the platform stability for takeoff.

The goal of the GLMAV consists of using an *ad hoc* launcher, light enough to be carried by a single person, so that it can be brought as fast as possible over the site, where it becomes operational for observation. This novel MAV is packaged into an envelope, thus constituting the launched projectile. When the projectile passes its apogee it is transformed into a coaxial helicopter. Its main mission consists of hovering over a limited zone for detailed observation and of transmitting video sequences to the ground station in real time. High-level orders are sent to the platform in order to provide its maneuvering capacities. After the mission has been accomplished, the GLMAV is recovered at any way point fixed before or during the mission.

From the description of the concept, it follows that the advantages of the GLMAV become evident; they are described as follows.

1) The necessary energy to bring the vehicle over the observed scene is provided externally by the launcher.

2) A very fast intervention is possible; indeed, our first investigations have shown that less than 15 s are needed to stabilize the vehicle over the observed scene [1].

3) The GLMAV components should withstand the acceleration reached in the launcher, making the platform very rigid and robust to mishandling.

TABLE I

STATISTICAL VALUES OF THE PROJECTILE LAUNCHING VELOCITY FROM BALLISTIC TESTS

Tests at 12 kJ, 100-m range	Mean (8 fires) [m/s]	58.21	Tests at 25 kJ, 500-m range	Mean (8 fires) [m/s]	103.59
	Standard deviation [m/s]	1.29		Standard deviation [m/s]	2.34
	Mean deviation [m/s]	1.14		Mean deviation [m/s]	1.99
	Variance	1.66		Variance	5.49

4) The acoustic discretion is ensured as the rotors start to operate only 6–7 s before the observation begins.

Given the dimensions and symmetry constraints imposed by the concept of gun-effect launching, by the rotational speeds involved and the planned missions, the use of two coaxial counter-rotating rotors is the solution that emerged implicitly.

Two observation scenarios are considered, with flights performed 100 m above the area located 100 to 500 m from the launch site. The GLMAV flight is split into three phases as follows:

1) the classical ballistic flight of a projectile;
2) the transient phase of the transformation of the projectile into an MAV with its slowdown;
3) the operational flight allowing hovering and maneuvering flight for the observation of the scene.

This paper only deals with the theoretical investigations and experimental validations of these three flight phases. However, the study of these flight phases requires the knowledge of technical information on the GLMAV system. These information are detailed in [11] for mechatronic aspects, in [17] for electronic aspects and summarized in Section II. The ballistic flight phase is studied in Section III, the transient phase in Section IV, and the operational flight in Section V. Section VI provides the conclusion.

II. GLMAV DESCRIPTION

Studies on aerodynamics, interior and exterior ballistics, and mechanics, detailed in [11] and summarized in the following three paragraphs, have converged toward the manufacturing of the dedicated ballistic launcher and of the platform.

The 80-mm-caliber ballistic launcher tested at the Institut Saint-Louis (ISL) proving ground has a mass of less than 10 kg with accessories, so that it can be transported by one person. The projectile acceleration in the tube does not exceed 2500 g, thus ensuring the survival of all the components embedded in the projectile. A series of tests analyzed in Table I validated the entire system for the both launching conditions for which the launching velocities are theoretically 57 and 100 m/s, respectively (Section III-B).

The study of the GLMAV platform comprises two aspects: the projectile mode for the ballistic flight phase and the MAV mode for the transient and operational flight phases. Numerical simulations of computational fluid dynamics (CFD) allowed the calculation of its aerodynamic coefficients. Table II reports the coefficients obtained for the chosen fin-stabilized projectile: C_D, C_L, and Cm are the drag, lift, and pitching moment coefficients, respectively. $CL\alpha$ and $Cm\alpha$ are the first derivatives of lift and pitching moment coefficients. Xcp is the abscissa of the center of pressure counted from the projectile nose and normalized by the projectile caliber. These coefficients are used to analyze the projectile stability and to investigate its ballistic trajectory (Sections III-A and III-B).

TABLE II

AERODYNAMIC COEFFICIENTS OF THE FIN-STABILIZED PROJECTILE AT MACH NUMBER OF 0.357

α [°]	C_D	C_L	Cm	$CL\alpha$	$Cm\alpha$	Xcp
0	0.237					
3	0.251	0.212	0.084	4.055	1.612	2.101
6	0.287	0.423	0.170	4.037	1.623	2.104
9	0.341	0.615	0.232	3.913	1.478	2.078

Fig. 1. Final version 2.0 of the GLMAV platform.

The final platform in the MAV configuration shown in Fig. 1 has an upper rotor diameter of 0.35 m, a lower rotor diameter of 0.25 m, and a mass of 1.05 kg. In projectile mode, the rotors are packaged into the shell and the four fins for ballistic stabilization are deployed. Near the apogee of the ballistic trajectory, the rotor platform slides into the projectile envelope, and both rotors, each with a pair of folded blades, are deployed. During the blade deployment phase, the rotors start to rotate in order to slow down the vehicle for the hovering flight.

Studies on electronics, optronics, and signal transmission, detailed in [17] and summarized in the following two paragraphs, enabled the GLMAV to be ready for the implementation of the guidance, navigation, and control functionalities detailed in this paper.

The embedded electronic architecture is designed for real-time control of the actuators based on command laws computed by the onboard processor, high-level instructions coming from the ground station and sensor measurements. The motherboard receives the high-level commands from the ground station computer via the ZigBee protocol. The main

Fig. 2. Photomontage of the concept of the GLMAV for detailed observation in urban environment.

task on the board consists of running the control loop for the stabilization and control of the drone at a fixed frequency of 100 Hz. Using the feedback from sensors, the control algorithms compute setpoints for actuators in order to follow the desired trajectory [18].

The embedded IG-500N inertial measurement unit (IMU) uses three gyrometers and three micro-electro-mechanical systems accelerometers, a three-axis magnetometer, a GPS, a barometer, and a data fusion filter to provide the attitude, velocity, and location of the vehicle in real time. The standard IG-500N is enhanced in order to reach an accuracy of 1° for roll and pitch estimates in critical environmental conditions and to withstand the launching acceleration.

Finally, Fig. 2 is a representation of the GLMAV concept. It shows the ballistic launcher, two positions of the GLMAV in ballistic mode, two locations of the GLMAV in the transient phase, one position in which the detailed observation is performed, the location of the platform recovery, and the ground station. The latter includes a laptop for GLMAV control and another for video display.

III. Ballistic Flight Phase

The ballistic flight of the GLMAV consists of launching it in projectile mode and in letting it fly freely until the deployment of the rotor platform, which occurs after its apogee.

The ISL designs and develops an exterior ballistics code based on a trajectory model of 6 and 7 degrees of freedom (DoF) in compliance with the North Atlantic Treaty Organization (NATO) Standardization Recommendation 4618. This code, named BALCO for BALlistic COde [19], aims at meeting the requirements of the new ammunition generations. The architecture of the trajectory calculation is built around the Runge–Kutta–Fehlberg 7th- and 8th-order integration schemes. Several earth models, atmosphere models, aerodynamics models, thrust and base-burn models, and guidance, navigation, and control models, all dependent on the studied application, are implemented. BALCO is validated for several classical projectiles.

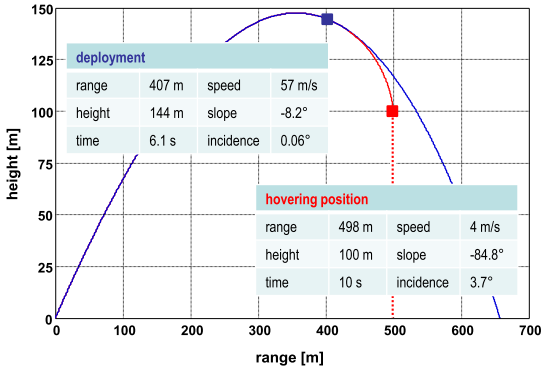

Fig. 3. GLMAV trajectory estimation.

A. Projectile Stability Analysis

A projectile is stable when the magnitude of its angular motion remains low during the flight: the projectile follows the curvature of the nominal trajectory; the latter can be predicted with accuracy. If the projectile is unstable, it switches completely during the flight, which greatly alters the trajectory. The projectile can be stabilized by spinning it (spin stabilized) or by fin deployment immediately after the projectile has left the tube (fin stabilized).

On the one hand, the stability analysis revealed that the projectile without fins was unstable. A spinning motion from 42 to 125 Hz should be given to the projectile for a launching velocity of 50 to 150 m/s, respectively. On the other hand, the stability analysis was possible by the analysis of CFD results presented in Table II. In fact, in the aerodynamic frame of reference, the first derivative of the pitching moment $Cm\alpha$ is positive, indicating the projectile stability. The fin-stabilized version was chosen, mainly as it was considered less complicated to deploy four small fins automatically than to cancel the spin motion of the projectile envelope during the slowdown phase.

B. Nominal Ballistic Trajectory Analysis

The fixed constraints are as follows: the maximum height of 150 m imposed by air traffic rules and the position where the observation flight starts, i.e., at a range of 500 m and a height of 100 m. The calculated trajectory corresponded to a muzzle velocity of 100 m/s and a vertical firing angle of 37°. The deployment position was estimated at a range of 407 m and a height of 144 m. This point was reached within 6.1 s, the vehicle velocity decreased to 57 m/s, the angle of attack was lower than 0.1°, and the vehicle slope angle was −8.2°. The negative slope angle meant that the vehicle flew nose down (Fig. 3, blue curve only).

The sensitivity of the nominal trajectory with respect to disturbances was evaluated for three parameters: 1) the presence of a side wind; 2) the transverse rotation of the projectile at the launch; and 3) the variation in the muzzle velocity. Trajectory calculations showed a side deviation of about 5 m in the deployment position for a side wind of ±5 m/s, which is acceptable as the side deviation can be compensated in the operational flight phase. Other trajectory calculations proved a side deviation of about 1 m in the deployment position for an

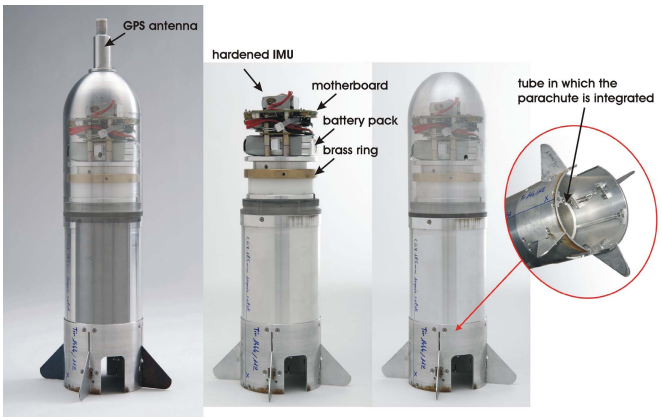

Fig. 4. Specific GLMAV for ballistic flight validation.

undesirable initial yaw speed of ± 1.5 rad/s. This disturbance amplitude is characteristic of the transverse rotation speed which can be transmitted to the projectile by the lateral motion of the tube during the launch. The variation in the muzzle velocity of ± 10 m/s led to a dispersion of about 30 m in the height of the deployment position, which was not acceptable. Therefore, a specific combustion chamber of the launcher [20] was designed in order to keep the muzzle velocity dispersion as low as possible (Table I).

C. Experimental Tests for Validation

This part is dedicated to the experimental validation of the ballistic flight alone. Specific projectiles were manufactured, respecting the geometry and the inertia distribution of the GLMAV version 2.0. A GPS antenna was added in front of the projectile (Fig. 4, left). The original electronics was embedded as well as a brass ring in order to respect the inertia distribution (Fig. 4, middle). During the flight, the electronics allowed the acquisition of the embedded sensor measurements from the IMU, the calculated angular position (Euler angles, quaternions), and finally the measured GPS coordinates. Given the cost of the IMU and the shooting conditions, the rotor platform was changed for a parachute system in order to softly recover the projectile (Fig. 4, right). It was initiated by a pyrotechnic device, triggered by an operator on the ground using a remote control [18].

Validation firings were executed at the ISL proving ground for three couples of elevation angles θ_0 and muzzle velocities V_0. A high-speed camera and a test pattern, both aligned with the launch axis, were installed at the barrel muzzle, thus allowing the visualization of the GLMAV exit. Fig. 5 presents a series of images proving the very good deployment of the fins when the GLMAV in projectile configuration left the barrel.

Fig. 6 shows the measurements by GPS of the trajectories of the GLMAV in projectile configuration under the following conditions: shot 1, $\theta_0 = 72°$ and $V_0 = 49$ m/s; shot 2, $\theta_0 = 50°$ and $V_0 = 69$ m/s; and shot 3, $\theta_0 = 35°$ and $V_0 = 96$ m/s. Three situations are visible as follows.

1) A first test in which no measurement took place. This situation lasted between 2 and 3.5 s. Indeed, after the projectile left the tube, it took the GPS sensor some time to get the measurements. The projectile acceleration and velocity did not affect the GPS performance.
2) A second test in which the end of the ballistic trajectory of the projectile was visible.
3) Finally, a third test with a more "diffuse" behavior of the flight phase under the parachute.

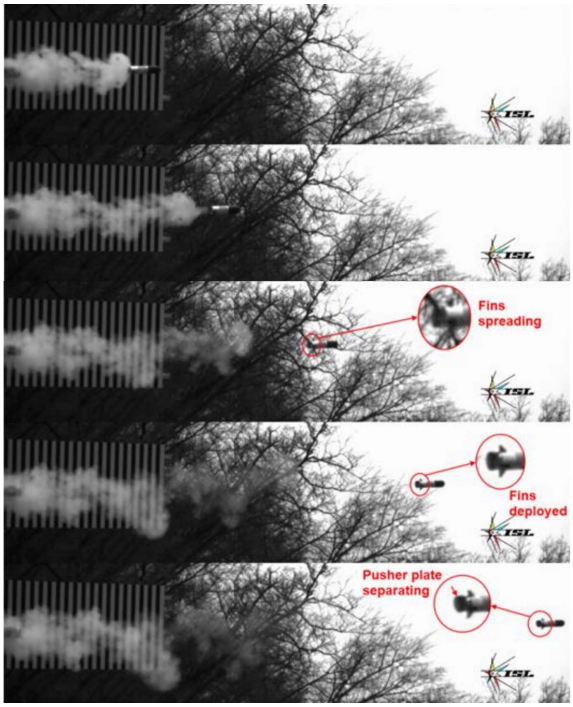

Fig. 5. Beginning of the GLMAV ballistic flight.

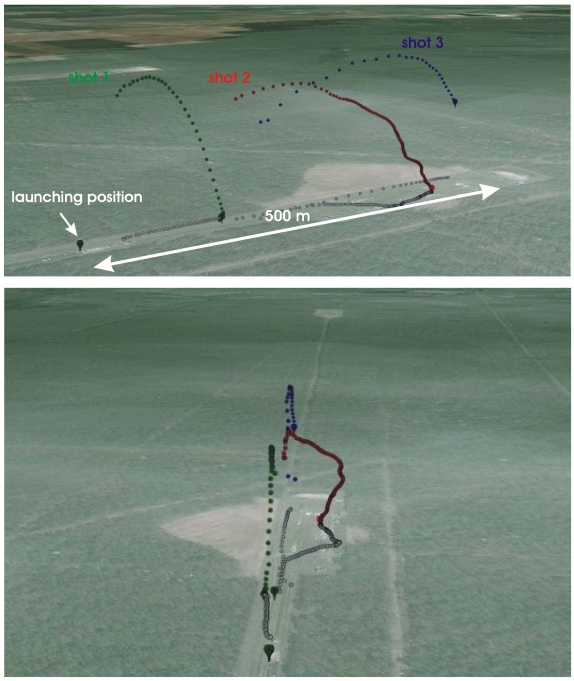

Fig. 6. GLMAV trajectory measurements by GPS acquisition.

The projectile stability was confirmed and the accuracy of the theoretical investigations of the trajectory was very satisfactory compared to the measurements performed by GPS.

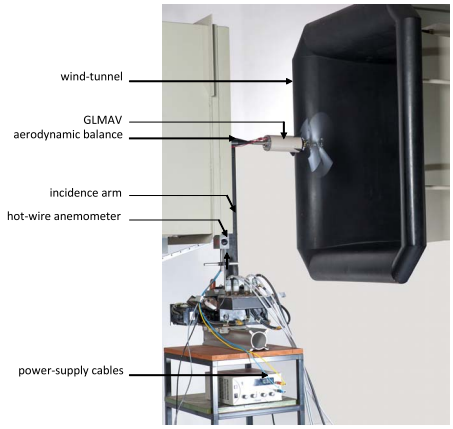

Fig. 7. Experimental setup in the continuous subsonic wind tunnel.

The measurement of the GLMAV position after 3.5 s of flight is a major result for the development of its autopilot.

IV. Transient Flight Phase

After the ballistic flight phase near the projectile apogee, the rotor platform is deployed. At this instant, the two counter-rotating rotors are operated to participate in the slowdown of the platform until the hovering flight phase is reached, enabling the stabilized observation of the scene. The vehicle slowdown is achieved by the concomitant action of the air resistance and of the thrust produced by the rotors; these two force components act in opposition to each other. This resulting force is known as the slowdown force. The air resistance is the force created by the obstacle consisting of the projectile envelope and the rotation of the rotors. Indeed, the rotating rotors can be considered to be more or less porous discs, depending on the rotor rotation speeds and having diameters of the rotors.

A. Experimental Identification of Forces and Moments

The aim consisted in experimentally quantifying forces and moments applied on the GLMAV in the presence of a wind acting against the development of the two rotor wakes. Therefore, tests were conducted in the ISL subsonic wind tunnel for different rotor rotation speeds and flow velocities. The influence of the GLMAV incidence was neglected.

The continuous subsonic wind tunnel has an open test section with a 70-cm width and a 90-cm height (Fig. 7). The flow velocity is adjustable from 0 to 40 m/s. It is adjusted by means of a hot-wire anemometer located in the converging portion of the wind tunnel. The turbulence level measured in the useful part of the test section does not exceed 0.25% for steady flows. The measurement of the six components of the aerodynamic torsor applied to the model during tests is conducted using an aerodynamic balance. Before each test campaign, the balance is calibrated using the ISL calibration bench.

The GLMAV platform mounted on the aerodynamic balance was maintained in the center of the wind-tunnel test section by means of an incidence arm (Fig. 7). Before each experiment, the incidence arm was set horizontally. The sideslip and yaw

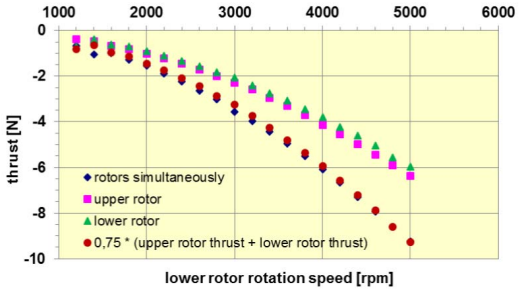

Fig. 8. Contribution of the thrust of each rotor in the absence of an incoming flow and total thrust.

angles of the arm were set to zero once for all when installing the setup. All commands and signals were transmitted to the GLMAV using the WiFi protocol. The entire operating range of the rotor rotation speed, determined during the development of the platform, was studied. The reference rotation speed was that of the lower rotor; it ranges from 1500 to 5000 rpm. At least five tests were carried out and the values presented corresponded to the mean of the measured quantities.

First, the thrust force produced by each rotor was measured for different rotation speeds in the absence of an incoming flow. The measurement was also carried out for the two rotors operating simultaneously. Fig. 8 shows these results as well as an approximation of the total thrust as a function of the thrust produced by each rotor. The thrust for the three series of measurements varied with the square of the rotation speed of the rotors, which is in agreement with the theory related to the lift created by a helix. The thrust of the lower rotor was substantially less than that of the upper rotor, which is due to the fact that the lower rotor ingests the wake of the upper rotor. Only 75% of the sum of the thrusts of the two rotors was compared with the thrust measured by the two rotors operating simultaneously. Thus, 25% of the thrust was absorbed by the interaction of the wake of the upper rotor with the lower rotor. A rotation speed of 5000 rpm for the lower rotor produced a total thrust of 9.5 N.

Second, during the transient and operational flights, it is essential to control the platform roll motion and in particular to determine the rotation speeds of both rotors so that their roll torques cancel each other out. Therefore, the upper rotor rotation speed was measured as a function of the rotation speed of the lower one at zero wind-tunnel velocity. The speeds of both rotors canceling the platform roll motion are proportional over the entire speed range and are expressed as follows:

$$\Omega_{\text{upp}} = 0.9\ \Omega_{\text{low}} \tag{1}$$

where Ω_{upp} and Ω_{low} represent the upper and lower angular rotor speeds, respectively. For all results, the angular rotor speeds were expressed as a function of the lower angular rotor speed. The law linking the angular rotor speeds was successfully verified in the presence of the incoming flow for different wind velocities (Fig. 9).

The absence of rotor rotation during the tests demonstrated the autorotation of the rotors. Indeed, for a flow velocity of about 10 m/s, when the blades were not driven by the motors, they began to rotate in the opposite direction to the

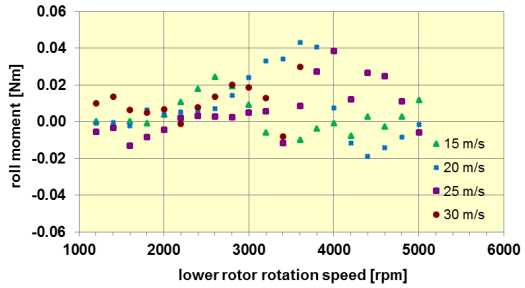

Fig. 9. Measurements in the subsonic wind tunnel: roll moment of the GLMAV as a function of the lower angular rotor velocity for different wind velocities.

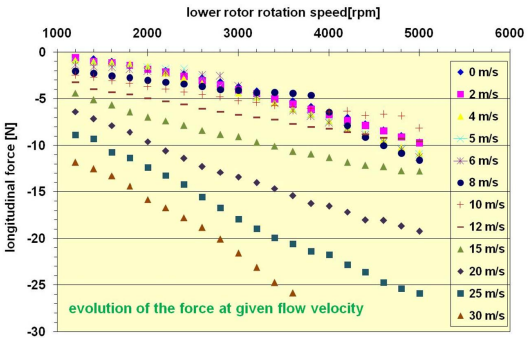

Fig. 10. Slowdown force measurements in the subsonic wind tunnel.

normal operation due to the relative incidence of the blades with respect to the flow. Thus, a significant resistive torque compared to the starting torque of the brushless motor made it impossible for the blades to rotate in the right direction. This problem is identified as a very critical point and requires special attention.

In any case, tests were carried out to measure the slowdown force applied to the platform as a function of the flow velocity and the rotor rotation speed. The maximum flow velocity was 30 m/s. Fig. 10 presents the average values of the slowdown force as a function of the lower rotor rotation speed for different flow velocities.

The slowdown force reaches higher values than the GLMAV mass force, which is beneficial to its slowdown. This force rapidly decreases with the decrease in the flow velocity. For a flow velocity higher than 10 m/s, the force decreases linearly with the rotor rotation speed. Below this flow velocity, a slope change is observed, indicating a change in the physics involved. Fig. 11 shows a close-up of the results for flow velocities from 0 to 12 m/s for a better view of the phenomenon. Data for 0 m/s correspond to the thrust, generated by the rotors without the incoming flow, which is the result of Fig. 8 in which the thrust is measured for both rotors. The only source of this force is the thrust created by the rotation of the blades.

Detailed flow visualizations with a high-speed camera were carried out in the wind tunnel in order to explain these singularity points in the slowdown force evolution. It turned out that the location of this sudden break in slope was the limit at which the air resistance made a significant contribution (or not) to the slowdown process of the platform. The conclusion is that the air resistance was the predominant contribution to the

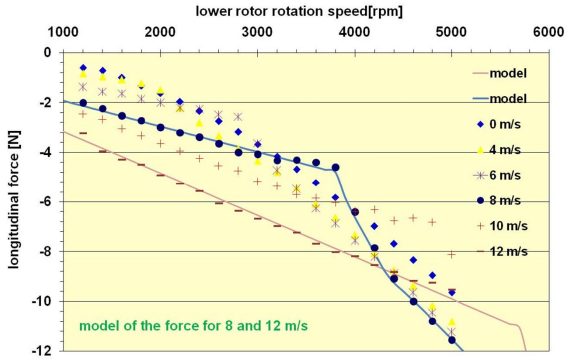

Fig. 11. Slowdown force measurements in the continuous subsonic wind tunnel and corresponding longitudinal force modeling.

slowdown force for the "flow velocity–rotor rotation speed" couple which was higher than that given by the slope breaking point.

B. Modeling of the Slowdown Force

This measurement mapping allowed the modeling of the slowdown force covering a wide range of flow velocities and rotor regimes. A modeling extension was proposed to cover the entire operating range that may occur in the slowdown phase (i.e., velocity from 60 m/s to 0).

The results depicted in Fig. 10 led to splitting the modeling into three distinct zones as follows:

1) One zone for rotor rotation speeds lower than the one located at the slope breaking point detected at flow velocities lower than 10 m/s; this zone is such as

$$\Omega_{\text{low}} < 480\, V_\infty. \tag{2}$$

2) One zone for rotor rotation speeds higher than the one situated after this breaking point; this zone is such as

$$\Omega_{\text{low}} > 480\, V_\infty + 500. \tag{3}$$

3) One zone for the transition between the two previous zones having an amplitude of 500 rpm, counted from the breaking line $\Omega_{\text{low}} = 480\, V_\infty$; this zone is such as

$$480\, V_\infty < \Omega_{\text{low}} < 480\, V_\infty + 500. \tag{4}$$

The evolution of the slowdown force $f(V_\infty, \Omega_{\text{low}})$ can be written in the following general form:

$$f(V_\infty, \Omega_{\text{low}}) = \alpha(V_\infty, \Omega_{\text{low}}) f_x(V_\infty, \Omega_{\text{low}}) + \beta(V_\infty, \Omega_{\text{low}}) f_T(V_\infty, \Omega_{\text{low}}) \tag{5}$$

$f_x(V_\infty, \Omega_{\text{low}})$ and $f_T(V_\infty, \Omega_{\text{low}})$ represent the contributions of the air resistance and of the rotor thrust, respectively. $\alpha(V_\infty, \Omega_{\text{low}})$ and $\beta(V_\infty, \Omega_{\text{low}})$ are coefficients ranging from 0 to 1. Detailed investigations resulted in the expressions used for the complete model of the slowdown force.

1) Model for the Zone Such as $\Omega_{low} < 480V_\infty$: The air resistance is predominant, the shape of the curves in Fig. 11 is linear and the modeling of the slowdown force can be performed by an affine function of the rotor rotation speed for

a given inflow speed. Hence, $\alpha(V_\infty, \Omega_{\text{low}}) = 1$ and $\beta(V_\infty, \Omega_{\text{low}}) = 0$ and the slowdown force is expressed by

$$f(V_\infty, \Omega_{\text{low}}) = f_x(V_\infty, \Omega_{\text{low}}) = a(V_\infty)\Omega_{\text{low}} + b(V_\infty) \quad (6)$$

where a and b are the functions of the flow velocity by the following linear regressions:

$$a(V_\infty) = -3.464193222 \cdot 10^{-6} V_\infty^2 - 9.5847058232 \cdot 10^{-5} V_\infty - 3.5468572317 \cdot 10^{-5} \quad (7)$$

$$b(V_\infty) = -1.4342810765 \cdot 10^{-1} V_\infty + 2.3558315372 \cdot 10^{-1}. \quad (8)$$

2) Model for the Zone Such as $480V_\infty < \Omega_{low} < 480V_\infty + 500$: The analysis shows an instability of the location of the breaking point in this zone. The contribution of the axial force is weighted by the coefficient $\zeta(V_\infty, \Omega_{\text{low}})$, ranging from 0 to 1. The relation (9) expresses the value of this coefficient for a good correlation with the experiments

$$\zeta(V_\infty, \Omega_{\text{low}}) = \left(\frac{\Omega_{\text{low}} - 480 V_\infty}{500} \right)^{\frac{1}{2}}. \quad (9)$$

The slowdown force is given by

$$f(V_\infty, \Omega_{\text{low}}) = f_x(V_\infty, \Omega_{\text{low}}) + \zeta(V_\infty, \Omega_{\text{low}})[f_T(\Omega_{\text{low}}) - 0.7 f_x(V_\infty, \Omega_{\text{low}})] \quad (10)$$

where $f_x(V_\infty, \Omega_{\text{low}})$ is provided by (6)–(8) and $f_T(V_\infty, \Omega_{\text{low}})$ is given by

$$f_T(\Omega_{\text{low}}) = -3.322407551 \cdot 10^{-7} \Omega_{\text{low}}^2 - 3.662625950 \cdot 10^{-4} \Omega_{\text{low}} + 0.41323540608. \quad (11)$$

3) Model for the Zone Such as $\Omega_{low} > 480V_\infty + 500$: Several modelizations show that the contribution of the air resistance due to the presence of the virtual rotor discs represents only 30% of the value of the force obtained in Section I. The relationship (11) is then used in this operating area

$$f(V_\infty, \Omega_{\text{inf}}) = 0.3 f_x(V_\infty, \Omega_{\text{inf}}) + f_T(\Omega_{\text{inf}}) \quad (12)$$

in which $f_x(V_\infty, \Omega_{\text{low}})$ is given by (6)–(8) and $f_T(V_\infty, \Omega_{\text{low}})$ by (11).

Finally, Fig. 11 proves that the model is in very good agreement with the experimental results. The average deviation of the model versus the measurement is 3.4% over all measured points, considering only the useful operating range during the slowdown phase.

C. Trajectory Simulations

The trajectory and characteristics of the transient phase were calculated using the slowdown force model. A 3 DoF version of the 6 DoF ballistic model was used, as the study was limited to the trajectory in a vertical plane. It was considered that the velocity and angle of incidence of the GLMAV at deployment time are known from the previous ballistic simulation (Section III). The initial conditions were the same as the ones of the previous 6 DoF simulation.

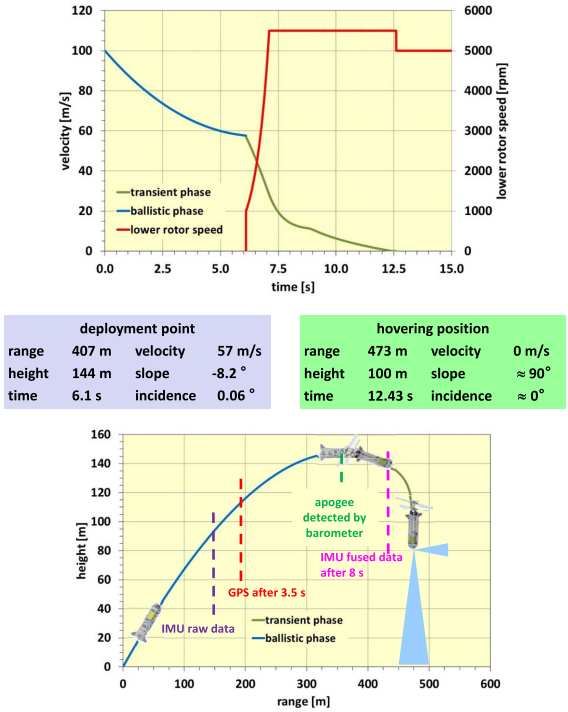

Fig. 12. Example of control law of the lower rotor motor and corresponding GLMAV velocity and trajectory.

Simulations showed that it was not necessary to immediately apply the maximum rotor rotation speed just after deployment. In fact, the slowdown force mainly generated by the air resistance at this moment, rapidly decreased the velocity from 57 m/s to around 10 m/s. They also showed that the lower rotor rotation speed had to be increased up to 5500 rpm to completely slow down the platform; indeed, at flow velocities less than 10 m/s, the slowdown force was of the same order of magnitude as that of the weight force of the platform. Thus, it became obvious that the slowdown of the platform was the most difficult task for descent velocities below 10 m/s during the transient phase.

Fig. 12 presents the GLMAV slowdown achieved. The top graph shows the control law of the lower rotor motor in red color and the corresponding platform velocity in blue and green colors for the ballistic and transient phases, respectively. The bottom graph shows the corresponding trajectory; the instants when sensor and GPS signals are received and when data are fused [21] are also indicated. During the ballistic phase ($0 \leq t \leq 6.1$ s), the rotors were embedded in the platform and therefore they did not turn. At the deployment point, the rotors turned by applying an exponential control law to the lower rotor ($\Omega_{\text{low}}(t) = 100\, e^{4t}$) during one second. Then, at $t = 7.1$ s, the maximum rotation speeds were reached and maintained to 5500 and 4950 rpm during 5.5 s for the lower and upper rotors, respectively. After 6.33 s of transient flight (12.43 s of total flight), the GLMAV platform was completely slowed down for the operational flight.

D. Experimental Validation of the Rotor Platform Deployment

Several series of tests in the subsonic wind tunnel were carried out with the complete GLMAV to verify the

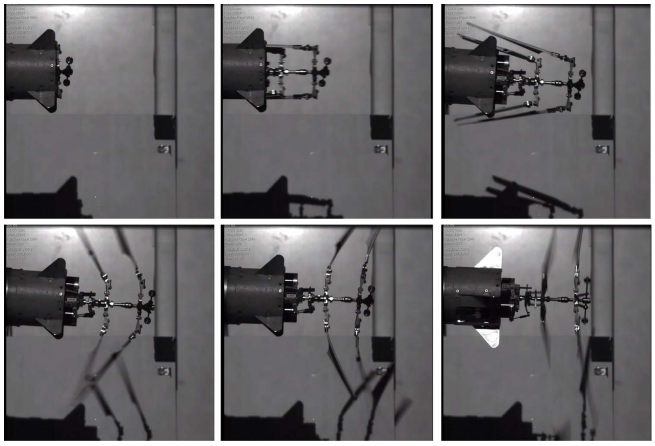

Fig. 13. Sequence of images demonstrating the proper rotor deployment for a flow velocity of 30 m/s.

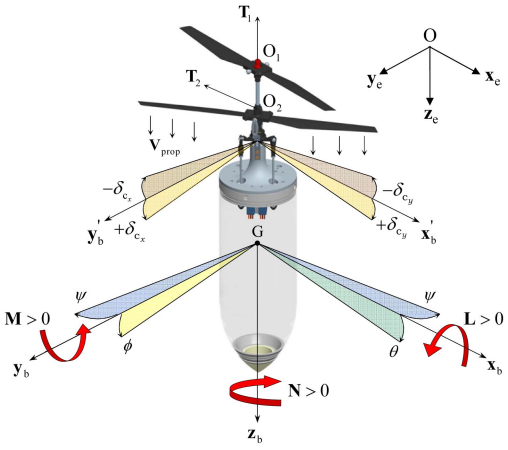

Fig. 14. GLMAV mathematical model.

deployment of the rotor platform. The vehicle was fixed inside a light support which allowed free roll and yaw motions of the vehicle. The rotor deployment was triggered when the selected flow velocity was reached. A high-speed camera recorded the sequence in order to demonstrate the proper rotor deployment (Fig. 13). Tests at a flow velocity of 30 m/s revealed that rotors began to turn 360 ms after triggering the deployment.

V. Operational Flight Phase For Observation

The operational flight allows hovering and maneuvering flight to be controlled for scene observation. The platform must be well stabilized in hovering flight so that the observer, located at the ground station, is able to immediately analyze the scene. The vehicle control is also important in maneuvering flight in order to accurately position the camera over the scene.

A. Mathematical Model of the GLMAV

The GLMAV mathematical model was built from the mechanics and aeromechanics physical laws. Miniature rotorcraft mathematical models can be divided into two submodels (i.e., an aerodynamic model coupled with a 6 DoF model) [22]. Hence, the main difficulty lies in the aerodynamic modeling which must be complete enough to accurately simulate the GLMAV dynamics and simple enough to develop control laws for autonomous flights. The great parameter variability makes it impossible to compile a complete mathematical model which captures all the aerodynamic effects. Fig. 14 shows the schematic of the GLMAV mathematical model. Starting from the modeling considered in [23] and [24], a detailed description is provided in [25] and [26] and recalled in the following sections for completeness.

1) 6 DoF Model: Considering the earth's coordinate system $\{O/\ \mathbf{x}_e,\ \mathbf{y}_e,\ \mathbf{z}_e\} = \mathcal{E}$ and the body coordinate system $\{G/\ \mathbf{x}_b,\ \mathbf{y}_b,\ \mathbf{z}_b\} = \mathcal{B}$ defined in Fig. 14, the transform matrix $\mathcal{R}_{\mathcal{B}\to\mathcal{E}}$ between the body coordinate system $\mathcal{B}$ and the earth's coordinate system $\mathcal{E}$ is expressed by the Euler angles as (13), as shown at the bottom of this page, ϕ, θ, and ψ are the roll, pitch, and yaw angles of the vehicle, respectively.

The kinematic parameters describing the GLMAV motions are composed of four vectors with three components each and they represent the system state as follows.

1) $\mathbf{x}(t) = [x(t)\ y(t)\ z(t)]^T$ and $\mathbf{V}(t) = [u(t)\ v(t)\ w(t)]^T$ are the location and velocity vectors of the gravity center, respectively, expressed in $\mathcal{E}$, the velocity vector including the wind effects.
2) $\boldsymbol{\varphi}(t) = [\phi(t)\ \theta(t)\ \psi(t)]^T$ is the vector of the Euler angles.
3) $\boldsymbol{\Omega}(t) = [p(t)\ q(t)\ r(t)]^T$ stands for the rotation speed between $\mathcal{B}$ and $\mathcal{E}$, expressed in $\mathcal{B}$.

The GLMAV is considered to be a rigid body having a fixed mass m and an inertia matrix J. Its gravity center is considered on the longitudinal $\mathbf{z}_b$-axis leading to a diagonal matrix. The diagonal terms I_{xx}, I_{yy}, and I_{zz} represent the inertia moment of the vehicle and furthermore $I_{xx} = I_{yy}$ for symmetry purposes.

The external force $\mathbf{F}(t)$ and moment $\mathbf{M}(t)$ applied to the vehicle are represented by vectors $\mathbf{F}(t) = [X(t)\ Y(t)\ Z(t)]^T$ and $\mathbf{M}(t) = [L(t)\ M(t)\ N(t)]^T$, respectively.

The motion equations of a rigid body are here composed of the kinematic equation of its gravity center position, of the equation resulting from the Newton theorem, of the kinematic equation of its attitude and of the equation resulting from the Euler theorem

$$\begin{aligned} \dot{\mathbf{x}} &= \mathbf{V} \\ m\dot{\mathbf{V}} &= \mathcal{R}_{\mathcal{B}\to\mathcal{E}}\ \mathbf{F} \\ \dot{\boldsymbol{\varphi}} &= \mathcal{R}_{\boldsymbol{\varphi}}\ \boldsymbol{\Omega} \\ J\dot{\boldsymbol{\Omega}} &= -\boldsymbol{\Omega}\times J\ \boldsymbol{\Omega} + \mathbf{M} \end{aligned} \quad \text{with } \mathcal{R}_{\boldsymbol{\varphi}} = \begin{bmatrix} 1 & \tan\theta\sin\phi & \tan\theta\cos\phi \\ 0 & \cos\phi & -\sin\phi \\ 0 & \dfrac{\sin\phi}{\cos\theta} & \dfrac{\cos\phi}{\cos\theta} \end{bmatrix}. \tag{14}$$

$$\mathcal{R}_{\mathcal{B}\to\mathcal{E}} = \begin{bmatrix} \cos\theta\cos\Psi & \sin\phi\sin\theta\cos\Psi - \cos\theta\sin\Psi & \cos\phi\sin\theta\cos\Psi + \sin\theta\sin\Psi \\ \cos\theta\sin\Psi & \sin\phi\sin\theta\sin\Psi + \cos\theta\cos\Psi & \cos\phi\sin\theta\sin\Psi - \sin\theta\cos\Psi \\ -\sin\theta & \sin\phi\cos\theta & \cos\phi\cos\theta \end{bmatrix} \tag{13}$$

2) Aerodynamic Model: The model of the external force $\mathbf{F}$ is split between the loads generated by the mass $\mathbf{F_{mass}}$, the coaxial counter-rotating rotors $\mathbf{T}$ including the blade incidence angles, and the forces induced by the body immersed in the airflow $\mathbf{F_{body}}$ (15). The gyroscopic moments induced by the counter-rotating rotors are neglected as they cancel each other out, assuming that the differential speed is not large enough to induce a significant gyroscopic moment, which is realistic in hovering flight

$$\mathbf{F} = \mathbf{F_{mass}} + \mathbf{T} + \mathbf{F_{body}}. \tag{15}$$

The mass force $\mathbf{F_{mass}}$ is written as

$$\mathbf{F_{mass}} = mg \begin{bmatrix} -\sin\theta\, \mathbf{x}_b \\ \cos\theta \sin\phi\, \mathbf{y}_b \\ \cos\theta \cos\phi\, \mathbf{z}_b \end{bmatrix}. \tag{16}$$

The thrust is the main force generated by the two rotors allowing the GLMAV to hover in the air. The upper rotor contributes only to the vertical thrust $\mathbf{T}_{\text{upp}} = \mathbf{T}_1$ that is directly proportional to the upper rotor aerodynamic coefficient α and to the rotation speed Ω_{upp}. The lower rotor generates both a vertical thrust with respect to the $\mathbf{z}_b$ base vector (β, Ω_{low}) as is the case with the upper rotor and two lateral forces due to the swashplate incidence angles with respect to the $\mathbf{x}_b$ and $\mathbf{y}_b$ base vectors. The expression of the lower rotor forces $\mathbf{T}_{\text{low}} = \mathbf{T}_2$ depends on the swashplate incidence angles (δ_{cx}, δ_{cy}). The total thrust $\mathbf{T}$ with respect to $\mathbf{z}_b$ could be computed using the sum of the two individual rotor thrusts $[\mathbf{T}_{\text{upp}}]\mathbf{z}_b$ and $[\mathbf{T}_{\text{low}}]\mathbf{z}_b$; however, in reality, this thrust is less than this sum, as there is a loss of aerodynamic efficiency due to airflow interactions, as stated by (1) in Section IV-A. Finally, the total force $\mathbf{T} = \sigma(\mathbf{T}_{\text{upp}} + \mathbf{T}_{\text{low}})$ generated by the rotors is written as

$$\mathbf{T} = \begin{bmatrix} -\beta\, \sin\delta_{cy}\, \cos\,\delta_{cx}\, \Omega_{\text{low}}^2 \mathbf{x}_b \\ -\beta\, \sin\,\delta_{cx}\, \Omega_{\text{low}}^2\, \mathbf{y}_b \\ \left(\sigma\, \alpha\, \Omega_{\text{upp}}^2 + \sigma\, \beta\, \cos\,\delta_{cx}\, \cos\,\delta_{cy}\, \Omega_{\text{low}}^2\right)\mathbf{z}_b \end{bmatrix}. \tag{17}$$

The loss coefficient σ is experimentally determined using (1). The developed expressions of the thrust aerodynamic coefficients α and β are the functions of the original thrust coefficients $C_{T\text{upp}}$ and $C_{T\text{low}}$, the rotor radii R_{upp} and R_{low}, and the air density ρ, such as

$$\alpha = C_{T1}\pi\, R_{\text{upp}}^4 \rho \text{ and } \beta = C_{T2}\pi\, R_{\text{low}}^4 \rho. \tag{18}$$

The body envelope is composed of a cylinder and a half-sphere. The body force $\mathbf{F_{body}}$ depends on the air density ρ, the diameter D, the length l, and surface S_c of the cylinder, the half-sphere surface S_s, the aerodynamic coefficients C_x, C_y, C_z, and the total airflow velocity $\mathbf{V}$. In the end, the expression of the force acting on the body is written as

$$\mathbf{F_{body}} = \begin{bmatrix} \frac{1}{2}\rho\, l\, D\, S_c\, C_x\, u^2\, \mathbf{x}_b \\ \frac{1}{2}\rho\, l\, D\, S_c\, C_y\, v^2\, \mathbf{y}_b \\ \frac{1}{2}\rho\, l\, D\, S_c\, C_z\, w^2\, \mathbf{z}_b \end{bmatrix}. \tag{19}$$

By knowing the force vector, the resultant moment vector is computed and thus the aerodynamic model is completed. It is assumed that the force generated by the body immersed in the airflow induces a negligible moment in a first approach. Indeed, the flow velocity from the coaxial rotors is far greater than that produced by the body displacement and the external wind. Consequently, the force components $\mathbf{F_{body}}\cdot\mathbf{x}_b$ and $\mathbf{F_{body}}\cdot\mathbf{y}_b$ are negligible, compared to $\mathbf{F_{body}}\cdot\mathbf{z}_b$. In addition, a strong wind gust is only considered to be a force acting on the whole body on account of its small dimensions; thus, only the forces generated by the rotors could lead to a nonzero resultant moment. The pitch and yaw moments M and L induced by the incidence angles of the lower rotor are calculated using the cross product of the distance vector (from the gravity center to the rotor rotation center $\mathbf{GO_2} = d\mathbf{z}_b$) with the lower rotor thrust vector. The roll moment N generated by each rotor is directly proportional to their respective aerodynamic coefficients γ_{upp} and γ_{low} and rotation speeds Ω_{upp} and Ω_{low}. Finally, the expression of the moment acting on the body is

$$\mathbf{M} = \begin{bmatrix} -d\,\beta\, \sin\,\delta_{cx}\, \Omega_{\text{low}}^2\, \mathbf{x}_b \\ d\,\beta\, \sin\,\delta_{cy}\, \cos\,\delta_{cx}\, \Omega_{\text{low}}^2\, \mathbf{y}_b \\ \left(\gamma_{\text{upp}}\, \Omega_{\text{upp}}^2 + \gamma_{\text{low}}\, \Omega_{\text{low}}^2\right)\mathbf{z}_b \end{bmatrix}. \tag{20}$$

3) Model Identification: The model identification followed the procedure used for the transient flight phase (Section IV). A model similar to the version 2.0, but weighing 0.3 kg, detailed in [26] and [27], was used (Section V-C). This simpler model was simplified by keeping only those parts that were useful for the operational phase. In the future, the model identification could be achieved by in-flight measurements.

B. GLMAV Autonomous Trajectory

1) Without Wind: Several control strategies were studied for the autonomous navigation of the GLMAV in the presence of external disturbances. At first, the PID [28]–[30], pole placement [30], linear–quadratic regulator [31], and H_∞ [32] methods were developed and compared. Other nonlinear control techniques ensuring the stability of the whole flight envelope were validated and tested. The input–output linearization [33], the sliding mode control [34], the backstepping approach [35], [36], and the hierarchical control design [37] were also developed and compared. Mathematical details, proofs, and simulations of all these approaches were detailed in [30]. Only the results obtained by the hierarchical nonlinear control that showed the best efficiency are presented.

This hierarchical nonlinear control architecture combines a high-level position control of the vehicle with a low-level attitude control. This is the common control architecture for most aerospace applications. The main difficulty in its design consisted of proving the stability of the closed-loop system, making therefore the subject of numerous studies [38]. This was achieved by using the properties of the previously mentioned backstepping approach. The analysis of (14)

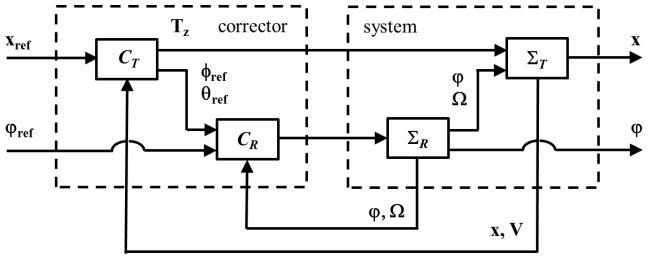

Fig. 15. Principle schematic of the hierarchical nonlinear control.

leads to the splitting of the translational and rotational dynamics into two interconnected subsystems $\sum_T$ and $\sum_R$ written as

$$\sum_T : \begin{cases} \dot{\mathbf{x}} = \mathbf{V} \\ m\dot{\mathbf{V}} = \mathcal{R}_{\mathcal{B}\to\mathcal{E}}\mathbf{F} \end{cases} \quad \text{and} \quad \sum_R : \begin{cases} \dot{\boldsymbol{\varphi}} = \mathcal{R}_{\varphi}\Omega \\ J\dot{\Omega} = -\Omega \times J\Omega + \mathbf{M}. \end{cases} \tag{21}$$

The equivalent schematic of the hierarchical control structure is given in Fig. 15. The output of the high-level loop controller C_T serves as reference for the low-level loop controller C_R.

The staging of the two dynamics was performed by a different selection of control gains, i.e., low gains for translational motion control and high gains for rotational motion control. Gains were adjusted by simulations in order to obtain the desired performance and limit the stress on actuators.

The objective of the backstepping control law synthesis has always to follow a trajectory $\mathbf{x_{ref}}$ and its successive derivatives with a specific orientation ψ_{ref} by influencing the signals $\mathbf{F} \cdot \mathbf{z}_b = Z$ and $\mathbf{M}$. As a consequence, the design procedure of a backstepping control led to building a Lyapunov function based on the errors of the $\mathbf{x}(t) - \mathbf{x_{ref}}$ location and $\psi(t) - \psi_{\text{ref}}$ orientation and of their derivatives. The mathematical details are provided in [30], [37], and [39]. According to different assumptions, the four control inputs Ω_{upp}, Ω_{low}, δ_{cx}, and δ_{cy} are calculated from (17), (20), and (21) and yield

$$\begin{aligned} \Omega_{\text{upp}}^2 &= (\gamma_{\text{low}}\mathbf{F}\cdot\mathbf{z}_b - \beta\,\mathbf{M}\cdot\mathbf{z}_b)/(\alpha\gamma_{\text{low}} - \beta\gamma_{\text{upp}}) \\ \Omega_{\text{low}}^2 &= (-\gamma_{\text{upp}}\mathbf{F}\cdot\mathbf{z}_b + \alpha\mathbf{M}\cdot\mathbf{z}_b)/(\alpha\gamma_{\text{low}} - \beta\gamma_{\text{upp}}) \\ \delta_{cx} &= -\mathbf{M}\cdot\mathbf{x}_b/d\beta\Omega_{\text{low}}^2 \\ \delta_{cy} &= -\mathbf{M}\cdot\mathbf{y}_b/d\beta\Omega_{\text{low}}^2 \end{aligned} \tag{22}$$

with $\mathbf{F}\cdot\mathbf{z}_b$ and $\mathbf{M}$ being the new control inputs to be determined.

The method starts by introducing the error variables

$$\begin{aligned} &\boldsymbol{\delta_1} = \mathbf{x} - \mathbf{x_{ref}}, \text{ the error in position,} \\ &\boldsymbol{\delta_2} = \mathbf{V} - \mathbf{V_{ref}}, \text{ the error in velocity,} \\ &\boldsymbol{\delta_3} = \boldsymbol{\varphi} - \boldsymbol{\varphi_{ref}}, \text{ the error in attitude,} \\ &\boldsymbol{\delta_3} = \mathcal{R}_{\varphi}(\Omega - \Omega_{\mathbf{ref}}), \text{ the error in angular velocity.} \end{aligned} \tag{23}$$

In the equations, $\mathbf{x_{ref}}$ and ψ_{ref} in $\boldsymbol{\varphi_{ref}}$ are the reference inputs and $\mathbf{V_{ref}}$, $\mathbf{a_{ref}}$, $\boldsymbol{\varphi_{ref}}$, and $\Omega_{\mathbf{ref}}$ are some virtual inputs described by

$$\begin{aligned} \mathbf{V_{ref}} &= \dot{\mathbf{x}}_{\mathbf{ref}} - k_1\boldsymbol{\delta}_1 \\ \mathbf{a_{ref}} &= \dot{\mathbf{V}}_{\mathbf{ref}} - \boldsymbol{\delta_1} - k_2\boldsymbol{\delta_2} \\ \phi_{\mathbf{ref}} &= a\tan\left(a_{\text{ref}_y}/\sqrt{a_{\text{ref}_x}^2 + (a_{\text{ref}_z} - g)^2}\right) \\ \theta_{\mathbf{ref}} &= a\tan(a_{\text{ref}_x}/(a_{\text{ref}_z} - g)) \\ \boldsymbol{\Omega_{\mathbf{ref}}} &= \mathcal{R}_{\varphi}^{-1}(\dot{\boldsymbol{\varphi}}_{\mathbf{ref}} - k_3\boldsymbol{\delta_3}). \end{aligned} \tag{24}$$

The control design, which guarantees that $\boldsymbol{\delta_i} \to 0$, consists of shaping the control inputs $\mathbf{F}\cdot\mathbf{z}_b$ and $\mathbf{M}$, as stated by the theorem of the hierarchical backstepping-based control law defined by

$$\begin{aligned} \mathbf{T}\cdot\mathbf{z}_b &= -m\sqrt{a_{\text{ref}_x}^2 + a_{\text{ref}_z}^2 + (a_{\text{ref}_z} - g)^2} \\ \mathbf{M} &= \boldsymbol{\Omega} \times J\boldsymbol{\Omega} \\ &\quad + J\,\mathcal{R}^{-1}[-\dot{\mathcal{R}}(\boldsymbol{\Omega} - \boldsymbol{\Omega_{\mathbf{ref}}}) + \mathcal{R}\dot{\boldsymbol{\Omega}}_{\mathbf{ref}} - \boldsymbol{\delta_3} - k_4\,\boldsymbol{\delta_4}]. \end{aligned} \tag{25}$$

The proof of this theorem is an application of Lyapunov's stability theory and LaSalle's invariance principle [36].

The performance of the hierarchical control was evaluated by simulations performed on the GLMAV dynamic model given by (14) with trajectory and yaw angle tracking. The temporal response of the closed-loop system (solid blue line) with respect to a reference trajectory (dashed red line) is shown in Fig. 16 for the gravity-center location and in Fig. 17 for the vehicle attitude. The system control inputs are depicted in Fig. 18 for the rotor angular velocities and in Fig. 19 for the swashplate angles.

Based on the complete set of results given in [30], the performance of the hierarchical nonlinear control algorithm is similar to that of the hierarchical backstepping control. However, the expressions of the control laws are less complex and thus easier to implement on the embedded computer.

2) In the Presence of Wind: In the case of wind gusts, which is more representative of outdoor conditions, it was mandatory to take into account the perturbations generated by the wind to guarantee the hovering flight. As there was no onboard wind measurement system, it was thus necessary to use perturbation estimators in order to readapt the control law and thus guarantee the stabilization of the GLMAV.

The external force $\mathbf{F}$ and moment $\mathbf{M}$ of (14) were identified by a specific estimation structure in order to ensure the exponential convergence of the estimation error. The unknown parameter estimations of the nonlinear form of the system were carried out by an estimation structure based on the research from [40] and [41]. However, in order to ensure the convergence of the estimators, it was necessary to assume that the dynamics of these disturbances were very low compared to the dynamics of the system.

The temporal response of the closed-loop system (solid blue line) with respect to a reference trajectory (dashed red line) is shown in Fig. 20 for the gravity-center location and in Fig. 21 for the vehicle attitude. The system control inputs are depicted in Fig. 22 for the rotor angular speeds and in Fig. 23 for the swashplate angles. Fig. 24 shows the perturbation estimation in terms of forces and moments. Note that the Euler angles are

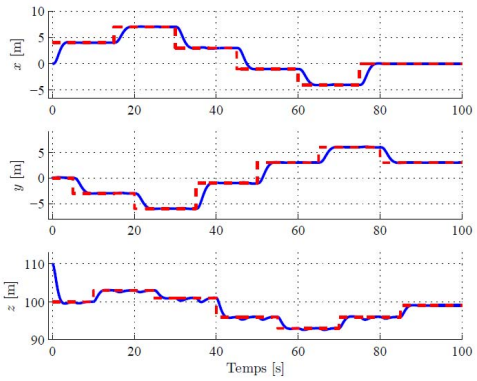

Fig. 16. Gravity-center location response (solid blue line) and its reference (dashed red line) for the hierarchical nonlinear control without wind.

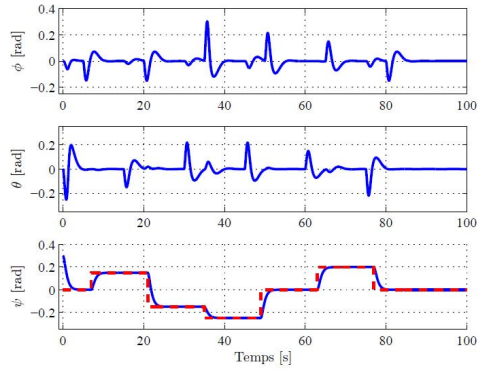

Fig. 17. Response of the Euler angles (solid blue line) and their references (dashed red line) for the hierarchical nonlinear control without wind.

nonzero in order to compensate for the perturbations effects. These simulation results clearly show that the tools used to allow the estimation of time-varying disturbances to a certain extent.

Again, the performance of the hierarchical nonlinear control algorithm is similar to that of the hierarchical backstepping control.

C. Control Law Implementation and Performance Evaluation

From a practical point of view, the hierarchical control algorithm was implemented on the simpler version of the GLMAV (Fig. 25). This version had rotor and electronic systems identical to those of the version 2.0; the shell in which the deployment system was embedded was removed. Indoor flights were performed in order to evaluate the performance of the control laws. It must be kept in mind that the robustness of a control algorithm is its ability to guarantee a certain level of performance and stability of the system with respect to uncertainties of its dynamic model.

Before starting tests, a detailed study was carried out on the influence of the uncertainties on the mass, on the inertia matrix, on the aerodynamic coefficients, on the sensors, on the occurrence of an actuator delay, and on the sampling frequency of the control law [30]. The vehicle mass should be known perfectly in order to avoid performance degradation in terms of trajectory tracking. Small variations in the inertia matrix as

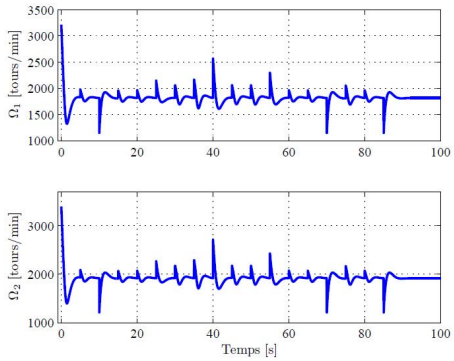

Fig. 18. Rotor angular velocities ($\Omega_{upp} = \Omega_1$, $\Omega_{low} = \Omega_2$) for the hierarchical nonlinear control without wind.

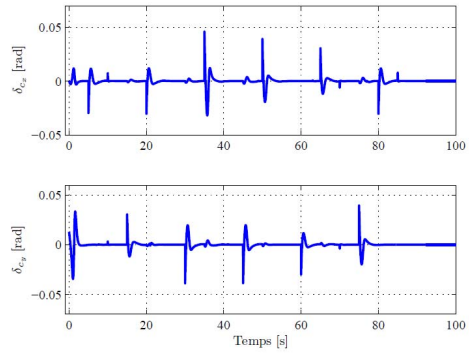

Fig. 19. Swashplate angles for the hierarchical nonlinear control without wind.

well as in the aerodynamic coefficients slightly affect the trajectory tracking. The hierarchical control approach is relatively insensitive to actuator delays. However, the trajectory tracking is influenced by noise and by the measurement delay of the sensors: they should be carefully characterized. Concerning the sampling frequency, the higher the sampling frequency, the better the performance of the trajectory tracking: the chosen sampling frequency of 100 Hz allowed a good compromise between the needs in the processing system resources and the performance obtained.

The experimental evaluation focused on the ability of the control law to ensure the proper execution of a position tracking operation, while maintaining a constant attitude around the yaw, as in the previous simulations. The time response of the closed-loop system with respect to the reference trajectory is given in Fig. 26 for the gravity-center location and in Fig. 27 for the attitude of the vehicle. The real vehicle behavior was less satisfactory than that obtained during the simulations. This performance degradation is likely to be due to uncertainties in the dynamic model, particularly coming from the aerodynamics and various noise measurements. It could also be due to the presence of a drift in the IMU measurement of the yaw motion, the IMU being particularly sensitive to magnetic disturbances.

D. Outdoor Tests

The validation of the aeromechanical architecture of the final version 2.0 of the GLMAV platform,

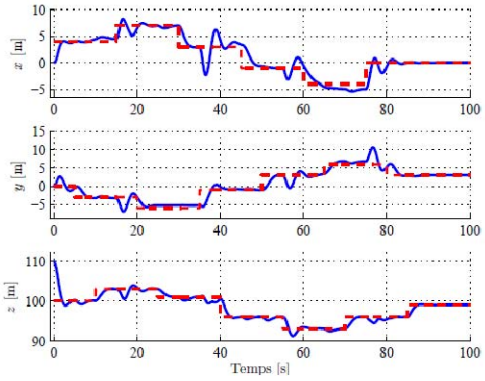

Fig. 20. Gravity-center location response (solid blue line) and its reference (dashed red line) for the hierarchical nonlinear control taking into account the perturbation compensation.

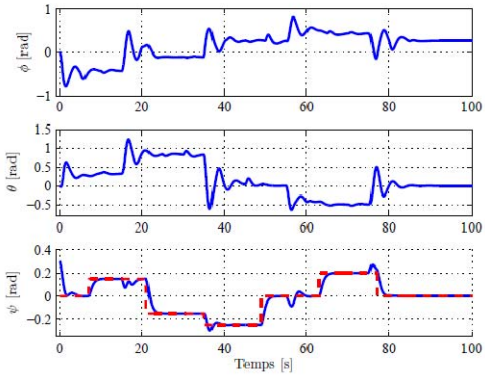

Fig. 21. Response of the Euler angles (solid blue line) and their references (dashed red line) for the hierarchical nonlinear control taking into account the perturbation compensation.

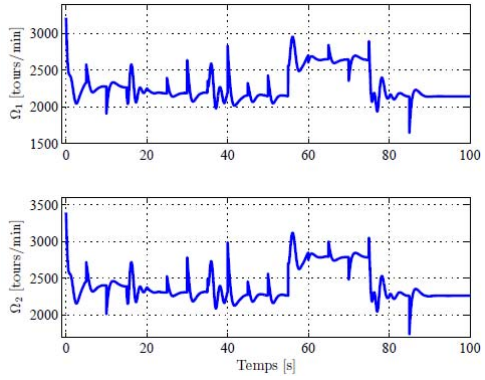

Fig. 22. Rotor angular velocities ($\Omega_{\text{upp}} = \Omega_1$, $\Omega_{\text{low}} = \Omega_2$) for the hierarchical nonlinear control taking into account the perturbation compensation.

manually steered in flight, is presented. The objective consisted of verifying its flight ability under different conditions.

Prior to the tests, the adjustment of the swashplate control-rod length was necessary so that the machine could maintain its position in the absence of roll/pitch commands. Each axis stabilization gain was adjusted to obtain a reactive stabilization while avoiding the oscillatory regime linked to excessive gain.

Flight tests were carried out indoors to overcome the

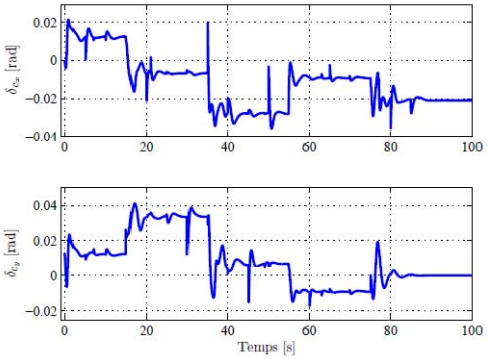

Fig. 23. Swashplate angles for the hierarchical nonlinear control taking into account the perturbation compensation.

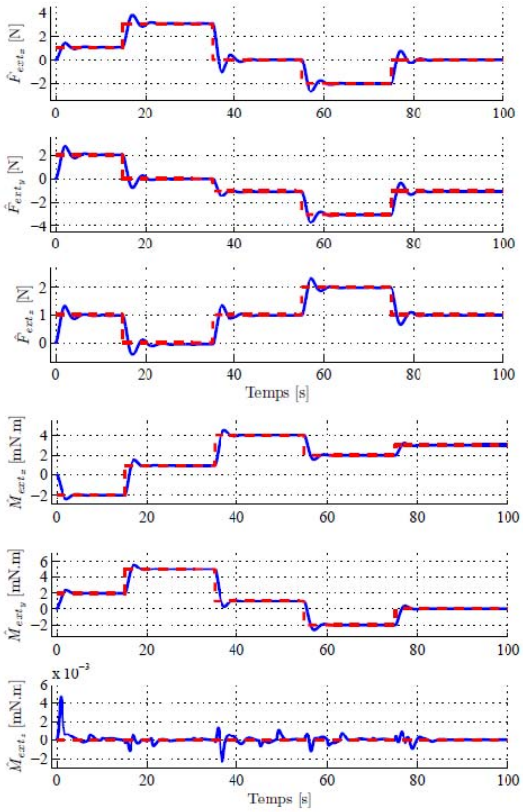

Fig. 24. Estimation of the force and moment vectors (solid blue line) and their references (dashed red line) with the hierarchical nonlinear control.

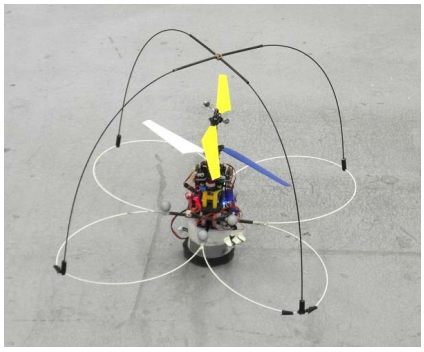

Fig. 25. Preliminary version of the GLMAV for control law implementation.

perturbations due to the wind and to make final adjustments for a stable hovering flight. Flight tests were performed outdoors without wind in order to manage maneuver flights. Other flight

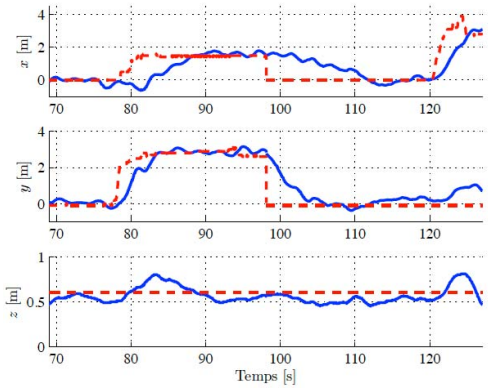

Fig. 26. Experimental test: gravity-center location response (solid line) and its reference (dashed line) measured with the preliminary prototype.

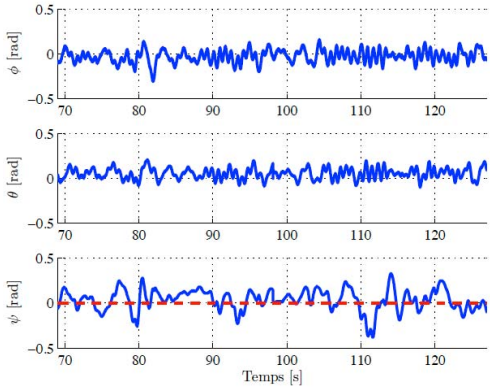

Fig. 27. Experimental test: response of Euler angles (solid line) and their references (dashed line) measured with the preliminary prototype.

Fig. 28. Photographs extracted from an outdoor flight sequence performed on the ISL proving ground.

tests were conducted with a wind having a force estimated at two according to the Beaufort scale [42].

Fig. 28 shows four photographs of an outdoor flight: when the GLMAV flew over the zone to be observed (top pictures), then when it approached the landing base and finally when it landed in the net composing the landing base. After changing or recharging the battery pack, the GLMAV was functional again.

These tests demonstrated the satisfactory GLMAV hovering and maneuvering flight in the absence of wind. The presence of wind made the control more difficult, due to the wind resistance of the platform. Despite this, it remained controllable and maneuverable. In hovering flight, when the platform tended to get carried away by the wind, the GLMAV had sufficient power resources to engage a translation against a wind force of two.

VI. Conclusion

A fully functional prototype of a GLMAV system was used for investigations on the ballistic, transient, and operational flight phases.

The ballistic, transient, and operational flight phases were investigated theoretically and experimentally in this paper. Indoor and outdoor tests of the system were successfully achieved. Ballistic flight tests proved the stability of the platform in the projectile mode and the availability of the IMU and GPS measurements for the autopilot.

Even if the complete transformation of the projectile into a helicopter has not been demonstrated yet, several important milestones were reached. The deployment and recovery of the vehicle thanks to a parachute were proved to be efficient, and onboard sensor data were recorded during the whole flight, allowing the navigation algorithms to be validated. Thanks to tests of the birotor in a wind tunnel for different wind and rotor speeds, a model of the aerodynamic effects on the rotor was built and is given in this paper. Deployments of the rotors in the wind tunnel were also conducted and the slowdown of the vehicle was achieved up to an axial speed of 30 m/s.

Contrariwise, the GLMAV hovering and maneuvering flight capabilities were highlighted. However, some critical points such as the wind surface area and balancing motions have still to be taken into consideration by the autopilot to achieve a fully automatic flight.

In the coming months, further studies will be conducted on the possibility of reducing the vehicle mass, while maintaining a prototype withstanding the launch acceleration, thus enhancing performance. Further and deeper investigations will be carried out on the transient flight phase in order to demonstrate the validity of the complete GLMAV concept.

Acknowledgment

The authors would like to thank the following contributors to this study: V. Gassmann, A. Koehl, B. Martinez, K. Meder, E. Pecheur, and E. Spieser from the French-German Research Institute of Saint-Louis; A. Drouot, H. Rafaralahy, and M. Zasadzinski from the CRAN; P. Castillo, C. Chauffaut, I. Fantoni, and L. Munoz-Hernandez from the HEUDIASYC laboratory; R. Syriani and A. Guinamard from the SBG Systems SAS company.

References

[1] P. Gnemmi and J. Haertig, "Concept of a Gun Launched micro air vehicle," presented at the 26th AIAA Appl. Aerodyn. Conf., Honolulu, HI, USA, 2008, paper 2008-6743.

[2] P. Gnemmi, S. Changey, M. Boutayeb, R. Lozano, and R. Siryani, "Conception and realisation of a demonstrator for a hybrid projectile/MAV system," in *Proc. Workshop Int. Scurit Globale (WISG)*, Troyes, France, Jan. 2010, pp. 26–27.

[3] M. Costello and A. Peterson, "Linear theory of a dual-spin projectile in atmospheric flight," *J. Guid., Control, Dyn.*, vol. 23, no. 5, pp. 789–797, 2000.

[4] L. Hainz and M. Costello, "Modified projectile linear theory for rapid trajectory prediction," *J. Guid., Control, Dyn.*, vol. 28, no. 5, pp. 1006–1014, 2005.
[5] D. Ollerenshaw and M. Costello, "Simplified projectile swerve solution for general control inputs," *J. Guid., Control, Dyn.*, vol. 31, no. 5, pp. 1259–1265, 2008.
[6] J. Rogers and M. Costello, "Control authority of a projectile equipped with a controllable internal translating mass," *J. Guid., Control, Dyn.*, vol. 31, no. 5, pp. 1323–1333, 2008.
[7] S. Theodoulis, V. Gassmann, P. Wernert, L. Dritsas, I. Kitsios, and A. Tzes, "Guidance and control design for a class of spin-stabilized fin-controlled projectiles," *J. Guid., Control, Dyn.*, vol. 36, no. 2, pp. 517–531, 2013.
[8] P. Browning *et al.*, "An experimental investigation of the transient effects associated with wing deployment during ballistic flight," *SAE Int. J. Aerosp.*, vol. 4, no. 2, pp. 1097–1105, 2011.
[9] J. Wilhelm, E. Jackson, P. Browning, W. Huebsch, V. Mucino, and M. Gautam, "Flight simulation of a hybrid projectile to estimate the impact of launch angle on range extension," in *Proc. Int. Mech. Eng. Congr. Expo. (ASME)*, 2012, pp. 615–620.
[10] J. Wilhelm, J. Close, W. Huebsch, and M. Gautam, "A de-spin and wings-leveling controller for a 40 mm hybrid projectile," *SAE Int. J. Aerosp.*, vol. 6, no. 2, pp. 683–692, 2013.
[11] P. Gnemmi *et al.*, "Conception and manufacturing of a projectile-drone hybrid system," *IEEE/ASME Trans. Mechatronics*, vol. 22, no. 2, pp. 940–951, Apr. 2017.
[12] M. Costello and E. Beyer, "Performance of a projectile/rotor kinetic energy reduction system," in *Proc. AHS Int. Specialist Meet.-Unmanned Rotorcraft, Design, Control Testing, Amer. Helicopter Soc. Int.*, Chandler, AZ, USA, 2007.
[13] UVision. *Hero 30 ISR*. Accessed: May 29, 2017. [Online]. Available: http://www.uvisionuav.com/portfolio/wasp/
[14] AeroVironment. *Switchblade*. Accessed: May 29, 2017. [Online]. Available: http://www.avinc.com/uas/adc/switchblade/
[15] O. Melara. *Horus*. Accessed: May 29, 2017. [Online]. Available: http://www.otomelara.it/products-services/robotics-systems/horus/
[16] Prioria Robotics Inc. *Maveric*. Accessed: May 29, 2017. [Online]. Available: http://www.prioria.com/maveric/
[17] S. Changey, E. Roussel, R. Syriani, L. Bernard, S. Schertzer, and P. Gnemmi, "Electronics and vision system of a projectile-drone hybrid system (GLMAV)," *IEEE Aerosp. Electron. Syst. Mag.*, Dec. 2016.
[18] E. Roussel, P. Gnemmi, and S. Changey, "Gun-launched micro air vehicle: Concept, challenges and results," presented at the Int. Conf. Unmanned Aircraft Syst. (ICUAS), Atlanta, GA, USA, May 2013.
[19] P. Wey, "BALCO 6/7 DOF trajectory model," presented at the 29th Int. Symp., Ballistics, Edinburgh, U.K., May 2016.
[20] J. Krcmar, C. Steinbach, and K. Dahhani, "Interior ballistics simulation of the two chambers GLMAV launcher," *Propellants, Explosives, Pyrotech.*, vol. 39, no. 5, pp. 768–773, Oct. 2014.
[21] C. Chauffaut, J. Escareno, and R. Lozano, "The transition phase of a gun-launched micro air vehicle," *J. Intell. Robot. Syst.*, vol. 70, nos. 1–4, pp. 119–131, Apr. 2013.
[22] R. Krashanitsa, G. Platanitis, D. Silin, and S. Shkarayev, "Aerodynamics and controls design for autonomous micro air vehicles," in *Proc. AIAA Atmos. Flight Mech. Conf. Exhib.*, Keystone, CO, USA, 2006, pp. 1277–1293.
[23] A. R. S. Bramwell, G. Done, and D. Balmford, *Bramwell's Helicopter Dynamics*. Oxford, U.K.: Butterworth-Heinemann, 2001.
[24] P. H. Zipfel, *Modeling and Simulation of Aerospace Vehicle Dynamics*. Reston, VA, USA: American Institute of Aeronautics and Astronautics, 2000.
[25] A. Koehl, H. Rafaralahy, B. Martinez, and M. Boutayeb, "Modeling and identification of a launched micro-air vehicle: Design and experimental results," presented at the AIAA Modeling Simulation Technolog. Conf., Toronto, ON, Canada, Aug. 2010.
[26] A. Koehl, "Modélisation, observation et commande d'un drone miniature à birotor coaxial," Ph.D. dissertation, Dept. Automat. Control, Univ. Lorraine, Longwy, France, Mar. 2012.
[27] A. Koehl, M. Boutayeb, H. Rafaralahy, and B. Martinez, "Wind-disturbances and aerodynamic parameters estimation of an experimental launched micro air vehicle using an EKF-like observer," presented at the 49th IEEE Conf. Decision Control, Atlanta, GA, USA, Dec. 2010.
[28] K. J. Åström and T. H. Hägglund, "PID controllers: Theory, design and tuning," in *International Society for Measurement and Control*. Research Triangle Park, NC, USA: Instrument Society of America, 1995.
[29] K. J. Åström and T. H. Hägglund, "Advanced PID control," in *The Instrumentation, Systems and Automation Society*. Research Triangle Park, NC, USA: Instrument Society of America, 2006.
[30] A. Drouot, "Stratégies de commande pour la navigation autonome d'un drone projectile miniature," Ph.D. dissertation, Dept. Automat. Control, Univ. Lorraine, Longwy, France, Dec. 2013.
[31] B. D. O. Anderson and J. B. Moore, *Optimal Control: Linear Quadratic Methods*. Englewood Cliffs, NJ, USA: Prentice-Hall, 1989.
[32] D. McFarlane and K. Glover, "A loop-shaping design procedure using H_∞ synthesis," *IEEE Trans. Autom. Control*, vol. 37, no. 6, pp. 759–769, Jun. 1992.
[33] J. J. Slotine and W. Li, *Applied Nonlinear Control*. Englewood Cliffs, NJ, USA: Prentice-Hall, 1991.
[34] C. Edwards and S. K. Spurgeon, *Sliding Mode Control: Theory and Applications*. New York, NY, USA: Taylor & Francis, 1998.
[35] M. Krstic, I. Kanellakopoulos, and P. Kokotovic, *Nonlinear and Adaptive Control Design*. Hoboken, NJ, USA: Wiley, 1995.
[36] A. Drouot, E. Richard, and M. Boutayeb, "An approximate backstepping based trajectory tracking control of a Gun Launched micro aerial vehicle in crosswind," *J. Intell. Robot. Syst.*, vol. 70, nos. 1–4, pp. 133–150, 2013.
[37] A. Drouot, E. Richard, and M. Boutayeb, "Hierarchical backstepping-based control of a Gun Launched MAV in crosswinds: Theory and experiment," *Control Eng. Pract.*, vol. 25, pp. 16–25, Apr. 2014.
[38] E. Panteley and A. Loría, "Growth rate conditions for uniform asymptotic stability of cascaded time-varying systems," *Automatica*, vol. 37, no. 3, pp. 453–460, 2001.
[39] V. Gassmann *et al.*, "Control of a gun-launched MAV for scene observation," presented at the 2nd IFAC Workshop Res. Edu. Develop. Unmanned Aerial Syst. (RED-UAS), Compiègne, France, Nov. 2013.
[40] P. Kudva and K. S. Narendra, "Synthesis of an adaptive observer using Lyapunov's direct method," *Int. J. Control*, vol. 18, no. 6, pp. 1201–1210, 1973.
[41] S. Sheikholeslam, "Observer-based parameter identifiers for nonlinear systems with parameter dependencies," *IEEE Trans. Autom. Control*, vol. 40, no. 2, pp. 382–387, Feb. 1995.
[42] *Echelle de Beaufort*. Accessed: Oct. 20, 2015. [Online]. Available: http://fr.wikipedia.org/wiki/%C3%89chelle_de_Beaufort

P. Gnemmi received the Engineer and Ph.D. degrees in mechanical engineering from the Conservatoire National des Arts et Métiers, Paris, France, in 1988 and 1993, respectively. He earned his accreditation on research management in mechanics-energetics from University Paris Nanterre La Défense, Paris, in 2012.

Since 1978, he has been with the French-German Research Institute of Saint-Louis (ISL), Saint-Louis, France, where he was an Engineer from 1989 to 1994, and a Research Scientist until 2010. He became the Head of the Aerothermodynamics and Shock Tube Laboratory of ISL until 2013, where he was the Manager of Research Projects until 2016. He became the Head of the Aerodynamics and Exterior Ballistics Group of ISL until 2017. He became the Head of the Division Flight Techniques for Projectiles in 2017. He has authored or co-authored around 80 archival journals or conference papers among 210 publications and he holds two patents. His current research interests include the whole range of fields allowing the study of non-guided and guided projectiles.

Dr. Gnemmi was a recipient of the "Prix Sciences et Défense" in 2001 awarded by the French Ministry of Defence. He was promoted "Chevalier dans l'Ordre des Palmes Académiques" in 2015.

S. Changey received the Engineer and master of science degrees from the Ecole National Supérieure de Physique de Strasbourg, University of Strasbourg, Strasbourg, France, in 2002, and the Ph.D. degree in automatic control from Supélec, University of Paris XI, Orsay, France, in 2005.

He joined the French-German Research Institute of Saint-Louis, (ISL) Saint-Louis, France, in 2002. From 2010 to 2013, he was the ISL scientific responsible for the gun launched micro-air vehicle project (GLMAV). Since 2014, he has been managing the ISL Navigation Project. The goal of this project is to manufacture an IMU (software and hardware) adapted to a gun-launched projectile. His current research interests include about ballistic and nonlinear estimation systems.

P. Wey received the M.E. degree from the Ecole Nationale Supérieure des Mines de Saint-Etienne, Saint-Étienne, France, in 1984.

He was in charge of the Guided Supersonic Projectile Project which focused on the guidance and control of fin-stabilized projectiles for air defense purposes. He is currently a Senior Research Scientist with the French-German Research Institute of Saint-Louis, Saint-Louis, France. He is currently in charge of the Electromagnetic Artillery System Project which combines EM railguns and hypervelocity projectiles. Since 2009, he has been leading the Team of Experts, North Atlantic Treaty Organization, in charge of defining a standard six and seven degree-of-freedom trajectory model for guided projectiles. Based on this model, he has developed the BALCO software which has been released as the NATO Technical Sharable Software. His current research interests include the design and development of simulation models in the field of exterior ballistics and the analysis of weapon systems performance.

Mr. Wey is a Senior Member of the International Ballistics Society and is a reviewer for the *Journal of Aerospace Engineering*.

E. Roussel received the master of science degree in electrical engineering from the Institut National des Sciences Appliquées, Strasbourg, France, and the master's degree in automatic control and robotics from the Ecole Nationale Supérieure de Physique de Strasbourg, Illkirch-Graffenstaden, France, in 2010. He is currently achieving his Ph.D. dissertation in the Guidance, Navigation, and Control Group with the French-German Research Institute of Saint-Louis (ISL), Saint-Louis, France, on the topic of modeling and automatic control of helicopter MAVs.

He was an Engineer with ISL, where he was in charge of the study and the development of the electronic system of the GLMAV demonstrator.

C. Rey received the Engineer degree (DEST) in measurement and instrumentation engineering from the Conservatoire National des Arts et Métiers, Paris, France, in 1999.

He joined the French-German Research Institute of Saint-Louis, Saint-Louis, France, in 1993. He is currently a Senior Engineer in charge of particle image velocimetry measurements in subsonic, supersonic, and hypersonic flows. He also develops an embedded generator for projectile steering by electric discharge generating plasma and he is responsible for measurements and visualizations of the plasma interaction with a supersonic flow. He is also in charge of flight tests and measurements on the gun launched micro-air vehicle demonstrator.

M. Boutayeb received the Electrical Engineer degree from the "Ecole Hassania des Travaux Publics," Casablanca, Morocco, in 1988, the Ph.D. and HDR degrees in automatic control from the University of Lorraine, Longwy, France, in 1992 and 2000, respectively.

From 1996 to 1997, he was a Fellow Researcher at the Alexander von Humboldt Foundation, University of Duisburg, Duisburg, Germany. From 1997 to 1999, he was a Researcher at the "Centre National de la Recherche Scientifique," Paris, France. From 1994 to 2002, he was an Associate Professor with the University of Lorraine, Longwy, France. From 2002 to 2007, he was a Full Professor with the University of Strasbourg, Strasbourg, France. Since 2007, he has been a Full professor with the University of Lorraine. He has authored or co-authored of more than 200 papers in international journals and conferences. His current research interests include identification, state estimation, and control of dynamical systems.

R. Lozano received the master of science degree in electrical engineering from Centro de Investigación y de Estudios Avanzados (CINVESTAV), Mexico City, Mexico, in 1977, and the Ph.D. degree in automatic control from the Laboratoire d'Automatique de Grenoble, Grenoble, France, in 1981.

From 1981 to 1989, he was with the Department of Electrical Engineering, CINVESTAV. He was the Head of the Section of Automatic Control from 1985 to 1987. He has held visiting positions at the University of Newcastle, Callaghan, NSW, Australia, from 1983 to 1984, the NASA Langley Research Center, Hampton, VA, USA, from 1987 to 1988, and the Laboratoire d'Automatique de Grenoble, from 1989 to 1990. Since 1990, he has been the CNRS Research Director with the University of Technology of Compiègne, Compiègne, France, where he was the Head of the Laboratory Heudiasyc UMR 6599 CNRS-UTC, Compiègne, France, from 1995 to 2007. His current research interests include adaptive control of linear, nonlinear systems, robot manipulators, passive systems, teleoperation, unmanned aerial vehicles, and autonomous underwater vehicles.

Dr. Lozano was an Associate Editor of the *Automatica* from 1987 to 2000 and he has beenan Associate Editor of the *International Journal of Adaptive Control and Signal Processing* since 1993.